Environmental Science & Technology

Article

Cite This: Environ. Sci. Technol. 2019, 53, 1471−1481

pubs.acs.org/est

Uptake and Translocation of Styrene Maleic Anhydride Nanoparticles in *Murraya exotica* Plants As Revealed by Noninvasive, Real-Time Optical Bioimaging

Tai-Ran Zhang,[†] Chuan-Xi Wang,[∥] Feng-Qin Dong,[§] Zhi-Yue Gao,[∥] Chao-Jie Zhang,[†] Xian-Juan Zhang,[†] Li-Min Fu,[*,†] Yuan Wang,[∥] and Jian-Ping Zhang[*,†]

[†]Department of Chemistry, Renmin University of China, Beijing 100872, China

[∥]Beijing National Laboratory for Molecular Science, State Key Laboratory for Structural Chemistry of Unstable and Stable Species, College of Chemistry and Molecular Engineering, and Academy for Advanced Interdisciplinary Studies, Peking University, Beijing 100871, China

[§]The Key Laboratory of Plant Molecular Physiology, Institute of Botany, Chinese Academy of Sciences, Beijing 100093, China

Supporting Information

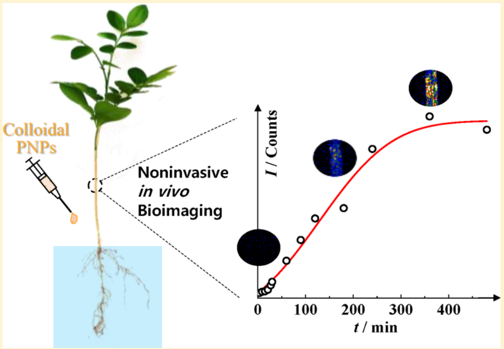

ABSTRACT: This work reports the in vivo uptake and translocation of PNPs in the one-year grown terrestrial plant, *Murraya exotica* (*M. exotica*), as investigated by two-photon excitation and time-resolved (TPE-TR) optical imaging with a large field of view (FOV, 32 × 32 mm^2) in a noninvasive and real-time manner. The PNPs ($\langle R_h \rangle$ = 12 ± 4.5 nm) synthesized from poly(styrene-*co*-maleic anhydride) (SMA) were Eu-luminescence labeled ($\lambda_L \approx 617$ nm). On exposing the roots of living *M. exotica* plants to the colloidal suspension of SMA PNPs at different concentrations, the spatiotemporal evolution of SMA PNPs along plant stems (60 mm in length) were monitored by TPE-TR imaging, which rendered rich information on the uptake and translocation of PNPs without any interference from the autofluorescence of the plant tissues. The TPE-TR imaging combined with the high-resolution anatomy revealed an intercell-wall route in the lignified epidermis of *M. exotica* plants for SMA PNP uptake and translocation, as well as the similar accumulation kinetics at different positions along the plant stems. We modeled the accumulation kinetics with Gaussian distribution to account for the trapping probability of a SMA PNP by the lignified cell walls, allowing the statistical parameters, the average trapping time (t_m) and its variance (σ), to be derived for the quantification of the PNP accumulation in individual plants. The TPE-TR imaging and the analysis protocols established herein will be helpful in exploring the mechanism of plant-PNP interaction under physiological condition.

1. INTRODUCTION

With the advancements of nanoscience and nanotechnology, functional nanomaterials have found a wide range of potential and practical applications.[1−4] Meanwhile, nanomaterials upon production and usage may enter the ecosystems,[5] and thus entail potential environmental and ecological consequences. Particularly, the uptake and translocation of nanomaterials by living organisms and the biological consequences have been crucial issues of scientific research.[6−11] It is well-known that plastic microparticles (PMPs, <10 μm) induce serious adverse biological effects to both marine and terrestrial organisms.[12−15] However, relatively little has been known for the ecological and biological consequences of plastic nanoparticles (PNPs, <100 nm) including man-made PNPs and those formed via degradation of plastic materials, an issue which receives increasingly high degree of scientific and social concerns.[16,17] Despite lacking of direct proof, it is believed that the PNPs may enter the atmospheric, aquatic, and soil environments via some propagation routes.[18−22] Compared to PMPs, PNPs may impose even more serious environmental and biological hazards, because their physical dimensions are less or comparable to the biomembrane structures and other cellular components.[23−30]

To assess the ecological and biological influence exerted by nanomaterials, it is critical to detect and analyze their uptake, translocation, deposition, and metabolism in various organisms. To this end, a range of analytical means have been used such as scanning electron microscopy (SEM),[31] transmission electron microscopy (TEM),[32] confocal fluorescence microscopy,[33] radioisotope labeling,[34] X-ray absorption spectroscopy (XAS),[35] inductively coupled plasma mass or optical emission spectrometries (ICP-MS or -OES),[32] and X-ray absorption near-edge structure analysis (XANES).[36] These methods,

Received: October 12, 2018
Revised: December 23, 2018
Accepted: January 3, 2019
Published: January 3, 2019

DOI: 10.1021/acs.est.8b05689

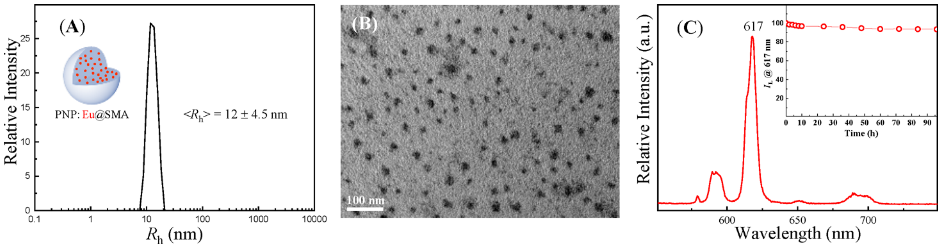

Figure 1. (A) Dynamic light scattering (DLS) data for Eu@SMA PNP (SMA PNP in short) colloidal solution. Inset shows schematic configuration of a SMA PNP. (B) TEM images of SMA PNPs stained with uranyl acetate. (C) Luminescence spectrum of colloidal SMA PNPs at the excitation wavelength of 400 nm. Inset depicts the photostability of SMA PNPs in colloidal solution (55 μg·mL^{-1}).

however, require the pretreatment of biological samples and hence mostly render in vitro information. In addition, the variation in the sensitivities and spatiotemporal resolutions often leads to discrepant conclusions. For instance, magnetometric analysis identified the uptake and translocation of Fe_3O_4 nanoparticles in pumpkin seedlings.[37] However, the same was not noted in an XAS study.[35] Fullerene C_{70} was concluded to be able to enter the leaf cells of rice as revealed by TEM and optical microscopy,[38] but it was found merely between the cell walls of onions in an independent TEM study.[39] Recently, the interaction of upconversion nanophosphors (UCNPs) with model plants has been monitored by the use of optical microscopy.[34,40] Because both the actinic light and the luminescence of rare-earth emission centers are in the near-infrared region, the optical imaging based on UCNPs is advantageous in minimizing the autofluorescence interference from biological tissues typically in the visible spectral region.

For in vivo imaging of PNP uptake by living organisms, optical confocal microscopy has been recently employed to investigate the deposition and metabolism of PNPs in green microalga,[41] zooplankton,[42] and zebrafish embryos,[43] which are relatively transparent objects. In addition, radioisotope labeling combined with autoradiography have been adopted to investigate the interaction of PNPs with scallop pecten maximus with high detection sensitivity.[44] The present work is intended to investigate the path and translocation dynamics of PNP uptake and accumulation in woody plants with a novel optical imaging method, which was recently developed based on a two-photon excitation and time-resolved detection (TEP-TR) scheme.[45] The TEP-TR imaging has been demonstrated to be capable of noninvasive and real-time visualizing the Eu-luminescence labeled PNPs in model animals with a wide field-of-view (FOV, 32 × 32 mm^2) and a large imaging depth (a few millimeters). In addition, the TEP-TR approach can completely reject the inherent autofluorescence from biological tissues including chlorophyll containing plant tissues, which enables the specific visualization of the Eu-luminescence labeled PNPs. It is therefore intriguing to further explore the potential application of TPE-TR imaging in monitoring the interaction of PNPs with plants under physiological conditions. In this context, two-photon microscopy has been recently employed to investigate the uptake of copper oxide nanoparticles by sweetpotato roots during postharvest treatment.[46] In contrast to TPE-TR imaging, this method relies on the selective detection of two-photon induced fluorescence from the lignin and the nanoparticles in biological tissues. The PNPs targeted in the present work were synthesized from poly(styrene-*co*-maleic anhydride) (SMA; see Figure S1 of the Supporting Information, SI, for molecular structure), a copolymer that is widely used in coatings, adhesives, emulsion dispersants, textile auxiliaries, printing inks, and other functional composite materials. In addition, we have recently shown that the SMA PNP is a promising nanocarrier for target-specific drug delivery.[47] That being stated, the one-year grown *Murraya exotica* (*M. exotica*), a terrestrial plant belonging to the evergreen shrub of Rutaceae family,[48,49] was chosen as our plant model for the following considerations: Since *M. exotica* plants grow rather slowly, their physical dimensions vary little over an experimental period that is typically scheduled to be a few days. The physical dimensions of the one-year grown *M. exotica* plants fit the FOV of TPE-TR imaging (cf. Materials and Methods).

We showed herein that the TEP-TR imaging could effectively reject the interference from the autofluorescence of plant tissues even containing intensely fluorescing chlorophylls, which allowed the real-time and noninvasive analysis of the accumulation and translocation processes of SMA PNPs in *M. exotica* plants under physiological condition. It was found that the uptake and translocation of SMA PNPs occurred in the lignified epidermis of a *M. exotica* plants, and that SMA PNPs accumulated essentially in phase in different sections along the plant stems. In addition, high-resolution anatomic analysis based on TEM and fluorescence lifetime imaging (FLIM) microscopy revealed an intercell-wall deposition of PNPs in the lignified epidermis, which together with the in vivo spatiotemporal evolution of SMA PNPs aqiured by TPE-TR imaging allow us to propose the route and mechanism of SMA PNP uptake and translocation, and to theoretically model the dynamics SMA PNP accumulation.

2. MATERIALS AND METHODS

2.1. Synthesis and Characterization of Eu-Luminescent Complex and SMA PNPs.

The Eu-luminescent complex, $Eu(TTA)_3BPT$ was synthesized as reported.[50] See Figure S1 for the molecular structure. It exhibits a luminescence quantum yield (Φ_L) of 43% at ~617 nm, a two-photon absorption cross section (δ_{2PA}) of ~150 GM at 800 nm (1 GM = 10^{-50} $cm^4 \cdot s \cdot photon^{-1} \cdot molecule^{-1}$), and an action cross section ($\Phi_L \cdot \delta_{2PA}$) of ~64 GM. The $Eu(TTA)_3BPT$-doped SMA PNPs (cf. inset of Figure 1A), were prepared by rapid mixing up $Eu(TTA)_3BPT$ and SMA solutions in a microchannel under reduced pressure.[47] As depicted in Figure 1A, the average hydrodynamic radius of SMA PNPs, $\langle R_h \rangle$, was determined by dynamic light scattering to be 12 ± 4.5 nm (Zetasizer Nano ZS90, Malvern, UK; 633 nm, 25 °C). The size of uranyl acetate stained SMA PNPs was further confirmed by TEM (JEM-1230; JEOL, Tokyo, Japan). It is seen in Figure 1B that the TEM morphology is in consistent with the R_h determined by dynamic light scattering. The overall action cross section of a SMA PNP particle

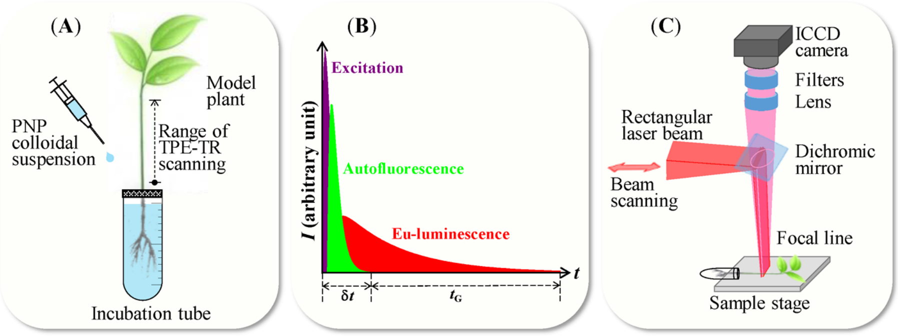

Figure 2. (A) Schematic drawing of a *M. exotica* plant cultivated in deionized water in an incubation tube. (B) Principle of autofluorescence rejection by TPE-TR imaging. (C) Schematic optical layout of the TPE-TR imaging apparatus.

containing ~46 Eu(TTA)$_3$BPT molecules was estimated to be $\Phi_L \cdot \delta_{2PA} \sim 1.1 \times 10^3$ GM. Figure 1C shows the luminescence spectrum of SMA PNPs in colloidal solution (55 μg·mL^{-1}) recorded with a fluorescence spectrophotometer (FL-980; Edinburgh Instruments Ltd., Livingston, U.K.). The inset of Figure 1C shows the time evolution profile of Eu-luminescence intensity for the colloidal solution. The <7% intensity drop over ~100 h proves an excellent photostability of the colloidal SMA PNPs, which is rather crucial for the application in kinetics analysis.

2.2. Target Plants. Both one-year grown plants and three-week grown seedlings of *M. exotica* were purchased from Sunshine Biology Ltd. (Beijing, China). The seedlings having unlignified epidermis were examined for a comparison to the plants with epidermis lignification. The full lengths from the root bottom to the leave top were 15−30 cm for the plants and 6−8 mm for the seedlings, while the stem diameters were 1.5−3.0 mm for the plants and 1−1.2 mm for the seedlings. The plants and seedlings as-received were grown in humus soil. After carefully removing the original growth media, they were cultivated in deionized water in a photosynthesis incubator (PRX-450C; Saifu Experimental Instrument Co. Ltd., Ningbo, China), which was thermostated at 25 °C under a humidity of 60% and a light flux of 6000 lx. Water for cultivation was prepared with a water purification system (Mingche TM-D 24UV; Merck Millipore Corp., Shanghai, China). Before being subjected to TPE-TR imaging, the plants or seedlings were cultivated in deionized water for 10 days to allow the self-healing of the possible hurts of the roots. Immediately before TPE-TR measurements, the roots of a *M. exotica* plant or a seedling were sealed together with appropriate volume of deionized water in a plastic tube for the convenience of TPE-TR imaging (cf. Figure 2A, C).

2.3. TPE-TR Imaging. The principle and instrumental details of TPE-TR imaging were presented elsewhere.[45] Briefly, as seen in Figure 2B, the TPE-induced autofluorescence from biochromophores can be rejected by detecting the Eu-luminescence after the glow of tissue autofluorescence. This can be realized by setting a proper delay time, δt, which is longer than the time span of autofluorescence (<100 ns) but much shorter than the Eu-luminescence lifetime (~0.62 ms). As shown in Figure 2C, after beam shaping and expansion, the beam of femtosecond laser pulses was focused into a line in the objective plane. The focal line with homogeneous power distribution was scanned over an objective plane, whereas the sample, the imaging optics and the intensified charge coupled detector (ICCD) remain static. By regulating the timing among pulsed excitation, scanning stepwise and ICCD sensing, the TPE-TR apparatus allowed a push-broom type, line-by-line imaging with a FOV of 32 × 32 mm^2 at a horizontal resolution of 60 μm. In a TPE-TR measurement for the present work, the femtosecond laser (120 fs, 800 nm; Solstice, Spectra physics, Santa Clara, CA, U.S.A.) was run at a repetition rate of $f = 500$ Hz with an average power of $P = 350$ mW. The typical time delay for autofluorescence rejection was $\delta t = 500$ ns, and the typical gate width of the ICCD imaging was $\Delta t_G = 1.8$ ms. The frame time was 4 s with the above running parameters.

2.4. Noninvasive, Real-Time Imaging of *M. exotica* Plants and Seedlings. An *M. exotica* plant together with its incubation tubes were loaded on the sample stage as schematically shown in Figure 2C. To start TPE-TR imaging, a volume of SMA PNP colloidal suspension was injected through the sealing cover into the incubation tube to reach a concentration of 55 μg·mL^{-1} and a total volume of ~5 mL. In this way, different concentration of SMA PNPs, 18 μg·mL^{-1}, 5.5 μg·mL^{-1}, and 1.8 μg·mL^{-1}, were applied to see the effect of concentration on the plant-PNP interaction. The moment of SMA PNP injection was taken as the timing to initiate the plant-PNP interaction, i.e. the time origin for the TPE-TR imaging. Note that this is a pseudo time origin for the real-time imaging, because it is hardly to know precisely the starting time of plant-PNP interaction. The typical SMA PNP exposure period for real-time TPE-TR imaging was 0−8 h. In the case of seedlings, we removed the incubation tube after certain period of exposing their roots to SMA PNP suspension, since two successive FOVs could cover the entire seedlings including the roots. Immediately before TPE-TR imaging, the seedlings were washed several times with deionized water to remove the physically adsorbed SMA PNPs. For the imaging of a plant, two successive FOVs could merely cover the stem. Therefore, the sample plant was placed together with its incubation tube on the sample stage, and only the stem was examined (Figure 2C). For convenience, a position close to the cultivation tube (the root) was taken as the spatial origin of the stem (Figure 2A). The TPR-TR measurements were done at 25 °C under a humidity of ~45% in a clean room.

2.5. Optical Microscopy and TEM. The horizontal resolution of the in vivo TPE-TR imaging (60 μm) is not enough to resolve the fine cellular structures. To further explore the location of SMA PNPs deposited in the tissues of plant and seedling, we performed in vitro optical microscopic and TEM characterizations. (i) For the evaluation of the degree of tissue lignification, the sections (thickness, 1 μm) of stems or seedlings of *M. exotica* were paraffin-embedded and safranin and fast-green stained, and were subjected to optical microscopic observation (TE-2000U; Nikon Corp., Japan). (ii)

DOI: 10.1021/acs.est.8b05689
Environ. Sci. Technol. 2019, 53, 1471−1481

To examine the deposition details of SMA PNPs, we carried out fluorescence lifetime imaging (FLIM) microscopy (Q2; ISS company, U.S.A.) for unstained cross-sectional slices (thickness, 200 μm) of the stems of *M. exotica* plants, whose roots were exposed to SMA PNPs for certain period (cf. Section 2.2). Taking advantages of the long Eu-luminescence lifetime (~0.62 ms), FLIM microscopy could discriminate the spatial distribution of SMA PNPs at a resolution of submicrometer. (iii) To facilitate the elucidation of the plant-PNP interaction mechanism, we investigated, using TEM, the precise locations of SMA PNPs with reference to the fine structures of cells at a subnanometer resolution. We fixed the segments of plant stems with 2.5% glutaraldehyde in 0.1 M phosphate buffer (PB, pH 7.2) over 4 h, washed them with cold PB for three times in 30 min, dehydrated them with a gradient of ethanol and cleared in acetone, and embedded them in spurr resin (SPI-CHEM). We then cut the segments into 1 μm-thick sections, which were stained with toluidine blue for the preview under an optical microscope. For electron microscopy, ultrathin sections (thickness, 70 nm) were cut with an Ultrotome (Leica EM UC7; Germany), mounted on Formvar-coated copper grids and poststained with uranyl acetate, and then observed with a TEM (JEM-1230; JEOL, Tokyo, Japan).

3. RESULTS

3.1. Autofluorescence Rejection by TEP-TR Imaging for the Chlorophyll-Containing Plant Tissues.

Figure 3 demonstrates the influence of autofluorescence on the TPE-TR images. As seen in panels B and E, without autofluorescence rejection ($\delta t = 0$ ns), the TPE-induced autofluorescence overwhelmed the images of the leaves and the stem. However, with $\delta t = 500$ ns the luminescence images originated from SMA PNPs are completely free from the autofluorescence interference (panels C and F). The excellent performance of autofluorescence rejection of TPE-TR imaging is crucial for the visualization of the in vivo spatiotemporal distribution of SMA PNPs especially in green plant samples. This point is further demonstrated by the TPE-TR images of an intact leaf of *M. exotica*: Without exposing to SMA PNPs, the leaf exhibited rather intense TPE-induced chlorophyll fluorescence when illuminated with the near-infrared femtosecond laser pulses (cf. Figure S2).

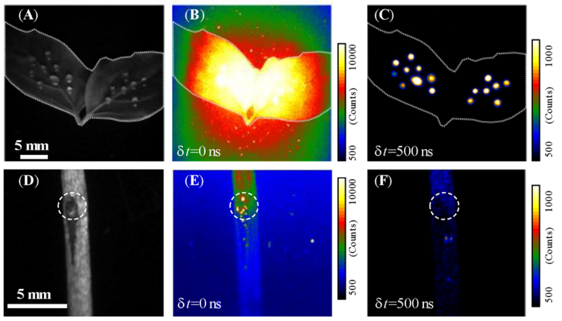

Figure 3. Upper and lower rows, respectively, show a pair of leaves and a stem segment of a one-year grown *M. exotica* plant. (A, D) Bright-field images, (B, E) TPE-TR images with $\delta t = 0$ ns, showing the overwhelming of the intense autofluorescence, (C, F) TPE-TR images with $\delta t = 500$ ns, illustrating the effect of autofluorescence rejection. In panels A−C, a few beads of SMA PNP colloidal suspension were put on the leaves. In panel F, the luminescence image was due to the uptake of SMA PNPs from the colloidal suspension (55 $\mu g \cdot mL^{-1}$; cf. Figure 2).

Figure 3D displays the bright-field image of a leaf-stem junction beneath a petiole, which appeared in green owing to the rich chlorophyll content as shown by the color photograph in Figure S2. The corresponding TPE-TR image in Figure 3E ($\delta t = 0$ ns) is distinctly different from that in Figure 3F ($\delta t = 500$ ns). Specifically, the bright spots in Figure 3E as highlighted by a circle are not seen in Figure 3F, meaning that these spots are false signals of autofluorescence. Notably, such false signals are suppressed completely by setting δt to 500 ns. Hereafter, the TPE-TR images for *M. exotica* plants and seedlings are those obtained with rejection of autofluorescence ($\delta t = 500$ ns). Besides autofluorescence rejection, the TPE-TR imaging is advantageous in its large imaging depth, which may differ for various plant tissues owing to the difference in tissue textures and chlorophyll contents. Our preliminary characterization showed that the imaging depths are >240 μm for the leaves and >300 μm for the stem cortexes of one-year grown plants, implying that the TPE-TR imaging can readily penetrate these types of plant tissues (cf. Figure S3).

3.2. Comparison of SMA PNP Uptake by the Seedlings and the Plants of *M. exotica*.

Figure 4B and C, respectively, shows the anatomic structures of the stem and the root of a *M. exotica* seedling. Upon safranin and fast-green staining, the cell walls rich in lignin appear in red, while those abundant in cellulose are seen in green. In the case of stem, the inner circular layer is the lignified xylem encircling a much less lignified pith. The cortex and epidermis outside this vascular bundle are clearly in green, indicating that the cell walls in this domain contain mainly cellulose rather than lignin. However, in the case of root, the central vascular cylinder is lignified, whereas the peripheral cortex and epidermis mainly contain cellulose.

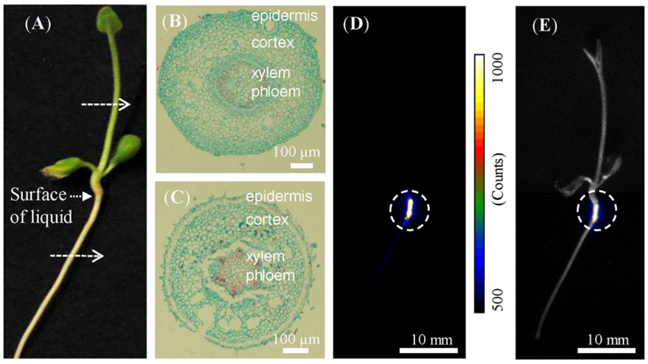

Figure 4. (A) Photograph of a *M. exotica* seedling. Optical microscopic images of the cross sections for (B) stem and (C) root of the seedling. The samples for optical microscopy were taken from the positions as indicated in panel A, and were paraffin-embedded and safranin and fast-green stained. (D) TPE-TR image of a *M. exotica* seedling and (E) its overlay with the bright-field image. Prior to TPE-TR imaging, the seedling roots was incubated in the colloidal suspension of SMA NPs (55 $\mu g \cdot mL^{-1}$) for 72 h. The dashed circles in panels D and E highlight the region around the surface of the incubation liquid as indicated in panel A.

Figure 4D and E shows the TPE-TR images of the seedling incubated with the colloidal solution of SMA PNPs for 72 h. The SMA PNPs are found merely around the differentiation zone. This domain was indeed around the solution surface during SMA PNP exposure. Therefore, the SMA PNPs are

DOI: 10.1021/acs.est.8b05689
Environ. Sci. Technol. 2019, 53, 1471−1481

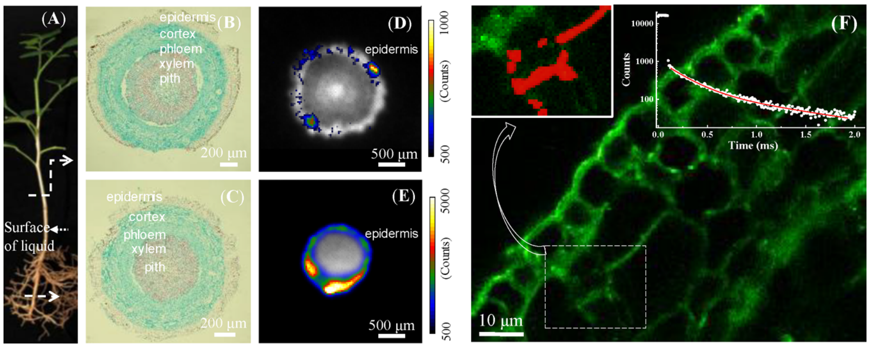

Figure 5. (A) Photograph of a *M. exotica* plant. Optical microscopic images of the cross sections of (B) stem and (C) root at the positions as indicated in panel A. The samples for optical microscopy were taken from the positions as indicated in panel A, and were paraffin-embedded and safranin and fast-green stained. The TPE-TR images of (D) stem and (E) root superimposed on their bright-filed images. Prior to TPE-TR imaging, the plant was incubated in the colloidal suspension of SMA PNPs (55 μg·mL^{-1}) for 72 h. (F) Confocal and FLIM microscopic images of the epidermis domain of the stem (excitation wavelength, 405 nm). The green contrast is the fluorescence image collected by ordinary confocal microscopy mode without lifetime discrimination. The upper left inset shows the FLIM image of SMA PNPs (red) overlapped with confocal image for the indicated region of interests (ROI). The millisecond lifetime-component of Eu-luminescence (cf. upper right inset) was used to extract the FLIM image.

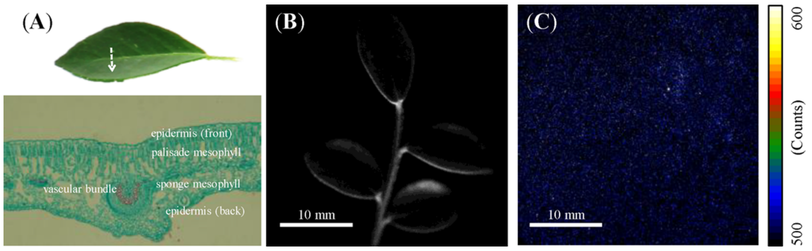

Figure 6. (A) Optical microscopic image of the cross section of the leaf taken from a one-year grown *M. exotica* plant. The sample for optical microscopy was paraffin-embedded, and safranin and fast-green stained. (B) Bright-field and (C) TPE-TR images of the leaves from a *M. exotica* plant incubated with colloidal suspension of SMA PNPs (55 μg·mL^{-1}) for 96 h. The image at a dark-count level was due to the lack of SMA PNPs and the autofluorescence rejection with a TPE-TR imaging delay of δt = 500 ns.

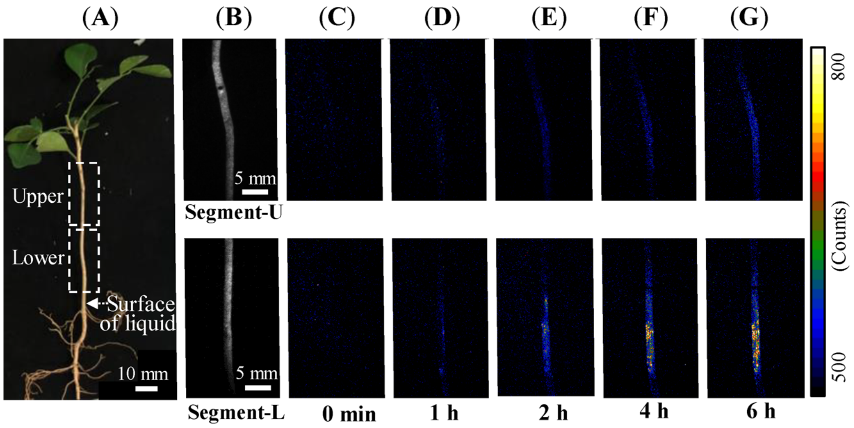

Figure 7. (A) Photograph of a one-year grown *M. exotica* plant. (B) Bright-field images of the lower (L) and the upper (U) segments of the stem. (C−G) Real time TPE-TR images recorded after injection of colloidal SMA PNP into the incubation tube to reach a concentration of 55 μg·mL^{-1}. The temporal origin was defined at the timing of injection (cf. Figure 2). More imaging details for the spatiotemporal evolution of accumulation SMA PNPs from 3 min to 8 h can be found in an SI Video.

most likely physically adsorbed onto the outer surface of epidermis, i.e., those could not be washed away. Taken the above results together, we conclude that the seedling roots are not active for the uptake of SMA PNPs from the colloidal solution, which is to be ascribed to the lack of lignification of the epidermis (see Discussions).

Figure 5B and C, respectively, shows the anatomic structures of a one-year grown plant of *M. exotica*. The epidermis of both root and stem are in red, indicating that the cell walls were lignified despite a relatively less lignification of the stem. In Figure 5D and E, the TPE-TR images are superimposed on their bright-field images. It is seen that the SMA PNP signals overlap intimately with the outmost layers of the bright-field images, which together with more detailed morphological analysis (cf. Figure S4) revealed that the SMA PNPs were localized in the epidermis. More details of the deposition of

SMA PNPs are illustrated in Figure 5F by comparing the confocal and the FLIM microscopic images of the epidermis. The upper left inset shows that the FLIM image of Eu-luminescence (red) overlapped intimately with the confocal microscopic image without lifetime discrimination (green), indicating that the PNPs deposited mainly in the domains of cell walls. Thus, for the one-year grown plant, in contrast to the three-week grown seedlings, the lignified epidermis of root and stem allow the uptake and translocation of SMA PNPs from the incubation suspension. In view of these TPE-TR and FLIM results, we can safely conclude that the lignified epidermis of *M. exotica* plant is active for the uptake and translocation of SMA PNPs.

The lignified-epidermis path of SMA PNP uptake also draws support from the TPE-TR imaging analysis of the leaves from a *M. exotica* plant. From the anatomic structures in Figure 6A, it is seen that the xylem of the vascular bundle is in red and hence is lignin containing, whereas the other tissues are unlignified. Figure 6B and C compares the bright-field and the TPE-TR images of the leaves. Judging from the rather low photon counts, which is close to the dark background, and in viewing of the imaging depth of leaves (~240 μm), we can conclude that the leaves contain undetectable SMA PNPs despite the long exposure period of 96 h for the mother *M. exotica* plant.

3.3. Noninvasive, Real-Time TPE-TR Dynamics of SMA PNP Uptake and Translocation by *M. exotica* Plants and the Effect of Exposure Concentration. Figure 7 shows a one-year grown plant of *M. exotica*, and its TPE-TR images recorded at selected timing. As seen in Figure 7D, SMA PNPs became visible after 1 h interaction of colloidal SMA PNPs in both the lower and the upper segments of the stem. From 2 to 6 h (Figure 7E−G), the SMA PNPs were continuingly enriched along the stem. Notably, the pattern of the lower segment seems more heterogeneous. The Eu-luminescence intensity reached the maximum at ~6 h, which is shown more clearly in Figure 8 where the Eu-luminescence intensity is plotted against position and timing. (See SI S5 for the procedures of data processing.) It is seen that the Eu-luminescence become recognizable around 0.5−1.0 h, and that the Eu-luminescence increase monotonically and evolve almost in phase at different locations along the stem.

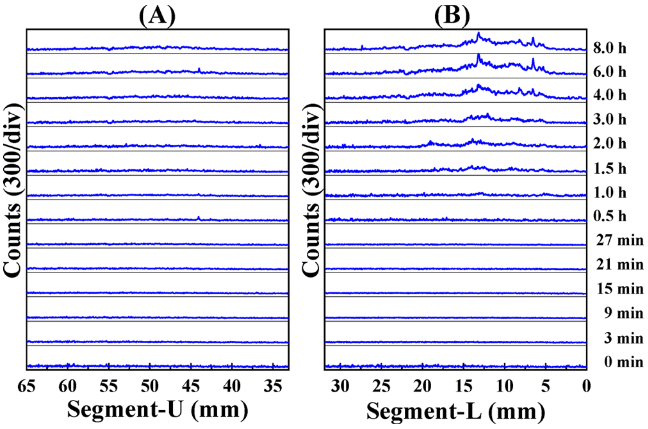

Figure 8. Plot of Eu-luminescence intensity of SMA PNPs along (A) the upper segment (Segment-U) and (B) the lower segment (Segment-L) of the plant stem at the indicated timing. Abscissa scale refers to the relative position from the starting point of TPE-TR scanning (cf. Figure 2A). The data were derived from the TPE-TR images as shown in Figure 7.

Figure 9A shows the time evolution profiles of SMA PNP accumulation at different positions along the stem of a *M. exotica* plant. From these kinetics curves, we estimated their rise-up timing at ~20 min. Although the maximal intensity are different at different positions, the kinetics curves simultaneously rise to their maxima in a similar time scale of 6−8 h. Such kinetics behavior is illustrated more clearly by normalizing the curves as shown in the inset of Figure 9A. For a phenomenological quantification of the kinetics, we fitted the curves in 20 min ~4 h to a linear model function, $I_L(t) = k \times t + I_0$, where k and I_0 represent the rate constant and the dark counts, respectively. The rate constants of the lower segment (0−30 mm), $k = 0.20 \pm 0.02\ \mathrm{h}^{-1}$, are found to be similar as those of the upper segment (40−60 mm), $k = 0.18 \pm 0.02\ \mathrm{h}^{-1}$, i.e., the accumulation of SMA PNPs at different positions evolved almost in phase.

To examine the concentration effect of SMA PNPs on the uptake and translocation dynamics of the one-year grown *M. exotica* plants, we systematically varied the SMA PNP concentration, and accordingly present the results of accumulation kinetics in Figure 9. The concentration effect can be characterized as the followings. (i) It is seen that, upon concentration decreasing, the luminescence intensity decreased systematically to an undetectable level (Figure 9D). The trend of descending of SMA PNP concentration, 55 μg·mL^{-1}, 18 μg·mL^{-1}, and 5.5 μg·mL^{-1}, holds a ratio of 10:3.3:1, which is in accord with the decrease tendency of the corresponding maximal Eu-luminescence intensity (I_L^m: 82, 25 and 7). This implies that the accumulation of SMA PNPs by the plant stems is linearly proportional to the exposure concentration in the aqueous phase. (ii) Reduction of the exposure concentration lead to substantially delayed rise-up time, e.g., from ~20 min (55 μg·mL^{-1}) to 2−3 hs (18 μg·mL^{-1}, 5.5 μg·mL^{-1}). However, the apparent timing to arrive at maximal Eu-luminescence intensity (I_L^m),~ 6 h, seems independent of the exposure concentration. (iii) Irrespective of the exposure concentration, the accumulation of SMA PNPs at different positions evolved almost in phase in terms of the rise-up and the saturation timing. Such kinetics behavior is to be rationalized by a physically meaningful model proposed for the uptake and translocation of SMA PNPs (cf. Discussion).

4. DISCUSSION

We have carried out noninvasive, real-time analysis of the in vivo uptake and translocation dynamics of SMA PNPs by PE-TR imaging the stems of one-year grown *M. exotica* plants, and have revealed the in-phase accumulation behavior of SMA PNPs at different positions along the plant stems under different exposure concentration. Our results favor a lignified-epidermis path of SMA PNP uptake and translocation. Herein, we will discuss on the uptake and translocation path and the mechanism on the basis of high-resolution TEM anatomic structures, and will model the unique spatiotemporal evolution dynamics so as to quantify the uptake and translocation processes of the individual living plants.

4.1. Path and Mechanism of SMA PNP Uptake and Translocation in Living *M. exotica* Plants. As shown by the TPE-TR imaging and the optical microscopic anatomy (vide supra), the root entry of SMA PNP uptake of the seedlings is inactive owing to the lack of epidermis lignification. However, the one-year grown plants bear the uptake path of

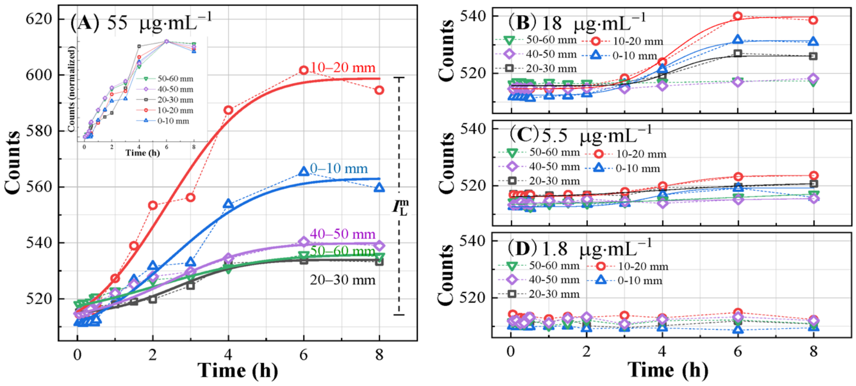

Figure 9. (A) Eu-luminescence kinetics for in vivo accumulation of SMA PNPs at different positions along the stem of a one-year grown *M. exotica* plant exposed to colloidal SMA PNPs at a concentration of 55 µg·mL^{-1}. Inset shows the normalized kinetics. These kinetics curves, each of which accounted for a stem section of 10 mm in length, were derived from the data in Figure 8. (B−D) Eu-luminescence kinetics for in vivo accumulation of SMA PNPs at different positions along the stems of one-year grown *M. exotica* plants at concentration of SMA PNPs (18 µg·mL^{-1}, 5.5 µg·mL^{-1} and 1.8 µg·mL^{-1}). For the convenience of intensity comparison, the vertical coordinates are displayed in the same scale (10 counts per division) in panels A−C. Maximal Eu-luminescence intensity ($I_{\mathrm{L}}^{\mathrm{m}}$) is defined as depicted in panel A. The solid curves were derived by fitting the kinetics curves to a model function (cf. eq 1).

SMA PNPs via the lignified root epidermis. Hereafter, the route and mechanism of SMA PNP uptake and translocation will be discussed with referring to the schematic anatomic structure of plant roots shown in Scheme 1.

Scheme 1. Root Anatomic Structure of a One-Year Grown *M. exotica* Plant[a]

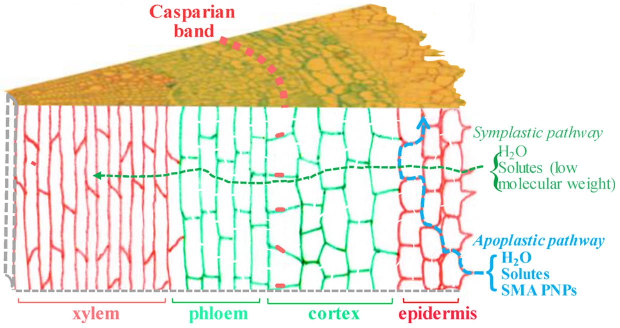

[a] Lignified and un-lignified cell walls are shown in red and green, respectively. Water and environmental nutrients and minerals can penetrate epidermis and cortex to reach the vascular cylinder for distant transport and distribution. The proposed lateral and ascent path for SMA PNP uptake and translocation is indicated by the dashed line in blue.

Apoplastic and symplastic pathways are two major routes responsible for the translocation of solutes through tissues or organs, both of which play critical roles for the interaction with environment (Scheme 1). Regarding the path of SMA PNP uptake for the roots of one-year grown *M. exotica* plants, the symplastic transport can be excluded, because otherwise SMA PNPs with an average hydrodynamic radius of 12 ± 4.5 nm would pass across the cortex, and eventually arrive at the vascular cylinder, and this is obviously not the case (Figure 5D and E). In addition, the cell-wall apoplastic route seems merely active for the epidermis of roots, because SMA PNPs were not found in the cortex and its encircled tissues. This together with the fact that no SMA PNPs were detected in seedlings and in plant leaves (Figures 4 and 6) point to the importance of epidermis lignification in forming the path of SMA PNPs: As shown by the anatomic structures of the *M. exotica* plants, the root epidermis is extensively lignified (Figure 5C). The cell walls in this case are rich in lignin (cross-linked phenolic polymers; cf. Figure S1), and hence the cell-wall apoplastic channels are mechanically rigid and relatively spacious.[51,52] In addition, there exist considerable amount of intercell-wall space owing to cell maturation upon cell-wall lignification. These extracellular channels and space facilitate the conduction of water, and thereby the translocation of hydrated SMA PNPs.

In the case of seedling, the cell walls of root epidermis are of little lignification (Figure 4C). Instead, they are abundant in cellulose (linear polysaccharide polymers; cf. Figure S1). Therefore, the cell-wall apoplastic channels are relatively flexible and hence prone to be compressed.[52] In addition, the epidermis cells of seedlings are proliferative, leaving less intercell-wall space. As such, the epidermis of seedling root does not allow the uptake and translocation of SMA PNPs. In the same token, the root cortex of both seedlings and plants do not allow the translocation of SMA PNPs.

For the one-year grown *M. exotica* plants, SMA PNPs were detected in the epidermis of both roots and stems in high concentration (Figure 5D and E). Following the root entry as depicted in Scheme 1, the extracellular cell-wall pathways can conduct the ascent translocation of SMA PNPs via the sap flow of living plants. To the contrary, in the roots and stems of *M. exotica* seedlings lacking of epidermis lignification, no SMA PNPs were detected (Figure 4D and E). In addition, SMA PNPs were not detected in the plant leaves owing to the deficiency in the extracellular apoplastic pathways (Figure 6).

We have provided strong evidence for the lignified epidermis path of SMA PNP uptake and translocation by TPE-TR imaging and optical microscopic anatomy, and especially by the FLIM microscopic image that could selectively visualize the SMA PNPs deposited in the cell walls (Figure 5F). However, it is still difficult to further distinguish the through-cell-wall and the intercell-wall paths. To make this clear, we examined in details the spatial deposition of SMA PNPs by using TEM with a subnanometer resolution. As shown in Figure 10, the TEM images of epidermis present a typical intercell-wall crevice with a submicrometer width (panel B and its ROI), as well as a typical triangular intercell-wall space with micrometer dimensions (panels C and D and their ROIs). In

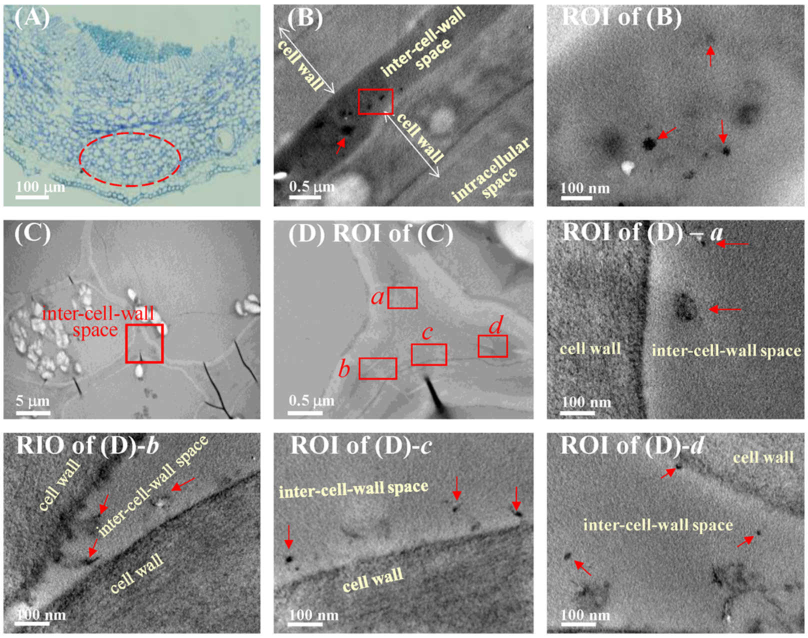

Figure 10. (A) Previewed optical microscopic image of a section of plant stem (thickness, 1 μm; toluidine blue stained). Dashed circle highlights the region to be examined with TEM. (B) TEM images for an ultrathin section of plant stem (thickness, 70 nm) showing the crevice between the cell walls. (C, D) TEM images for an ultrathin section of plant stem (thickness, 70 nm) showing the triangular intercell-wall space. The ROIs of panels B–D are displayed in high resolution, where the arrows in red point to the dispersed or clustered SMA PNPs. The *M. exotica* plant for the optical and the TEM analysis was incubated with colloidal suspension of SMA PNPs (55 μg·mL^{-1}) for 8 h. (See Figure S11 for the TEM images of control.)

Table 1. Parameters Derived by Least-Square Fitting of the Kinetics Curves in Figure 9A to the Model Function Eq 1

kinetics parameters	stem position (mm)				
	0–10	10–20	20–30	40–50	50–60
t_m (h)	2.5 ± 0.3	2.4 ± 0.2	2.6 ± 0.2	2.4 ± 0.3	2.1 ± 0.5
σ (h)	1.9 ± 0.5	1.7 ± 0.4	1.4 ± 0.3	1.8 ± 0.3	2.3 ± 0.5
I_L^m (counts/pixel)	57.2 ± 6.6	91.1 ± 7.9	19.4 ± 1.1	27.4 ± 2.0	22.3 ± 3.6

both cases, SMA PNPs in the ROIs are distinctly identified with morphologies comparable to those characterized in vitro by TEM (Figure 1B). Interestingly, as shown by the ROIs of higher resolution (with 100 nm scale bars), a substantial amount of SMA PNPs are in close proximities of cell walls, suggesting the adsorption/desorption binding mode of SMA PNPs. On the basis of the TEM and optical anatomy and the TPE-TR analyses, we conclude the intercell-wall path, rather than the through-cell-wall route, for the uptake and translocation of SMA PNPs in the lignified epidermis of *M. exotica* plants.

4.2. Spatiotemporal Evolution and Accumulation Mechanism of SMA PNPs in Living *M. exotica* Plants.

As illustrated by Figures 7 and 8 (see also the SI Video for more imaging details of the spatiotemporal evolution SMA PNP accumulation from 3 min to 8 h), the patterns of SMA PNP distribution along the stem are nearly unvaried with elapsing time. In addition, the Eu-luminescence intensity evolve almost in phase at different position as proved by the kinetics curves in Figure 9. These spatiotemporal characteristics imply that the SMA PNPs visualized by TPE-TR imaging are those localized in the epidermis. Therefore, the evolution kinetics essentially reflect the trap processes of SMA PNPs. Alternatively, for the SMA PNPs free in the mobile sap (water), their contribution to the Eu-luminescence intensity, if any, must be rather small, which is most likely due to a low concentration. This is confirmed by TPE-TR imaging of a two-orders-of-magnitude diluted colloidal suspension in a capillary (0.55 μg·mL^{-1}), which exhibited a photon count comparable to that of a plant stem with an accumulation time as long as 2 h (Figure S6).

In general, the sap flow velocity for wood plants is a few millimeters per minute with an upper limit of 10 mm·min^{-1},[53] meaning that within 20–30 min a 60–100 mm length of the stem can be flowed over with a moderate sap velocity of 3–5 mm·min^{-1}. However, the diffusion of SMA PNPs into stationary water in capillary is extremely slow (Figure S7). Therefore, the SMA PNPs translocating in a stem is concluded to be driven by the sap flow. Two different types of SMA PNP trap sites in the intercell-wall apoplastic channels are expected: (i) Those on the surface of lignified cell walls facing relatively large intercell-wall space, i.e., from a few hundred nanometers to a few micrometers (Figure 10B and D and the associated ROIs), where SMA PNPs experience dynamics adsorption and desorption. (ii) Those in rather narrow intercell-wall spaces, i.e. comparable to or below 100 nm (Figure 10, ROI of (D)-*b*), where the adsorption and desorption of SMA PNPs can be relatively slow due to the nanochannel restriction to the sap flow. As inspired by the random walk model for the dynamic adsorption/desorption of molecules in chromatography,[54] we modeled the SMA PNP accumulation kinetics of living plant stems by the use of an integral of Gaussian probability density,

DOI: 10.1021/acs.est.8b05689
Environ. Sci. Technol. 2019, 53, 1471–1481

$$I(t) = \frac{I_{\mathrm{L}}^{\mathrm{m}}}{\sigma\sqrt{2\pi}} \int_0^t e\frac{(\tau - t_{\mathrm{m}})^2}{2\sigma^2}\, \mathrm{d}\tau, \qquad (1)$$

where $I_{\mathrm{L}}^{\mathrm{m}}$ represents the maximal Eu-luminescence intensity, t_{m} stands for the average time for a SMA PNP particle to find a trap site, and σ is the standard deviation. These parameters can be derived by fitting the kinetics curves to the model function eq 1. As shown in Figure 9A, this model could well account for the experimental kinetics. The results thus obtained are listed in Table 1.

Compared to the linear model description of the kinetics curves (Section 3.3), the model function eq 1 provides a physically meaningful quantification of the kinetics, and hence a deeper insight into the uptake and translocation mechanism of SMA PNPs: When the intercell-wall trap sites in epidermis begin to capture SMA PNPs, the time for a particle to be captured must be relatively short, because most of the trap sites are open. Subsequently, the trap time becomes longer because of the reduced trap density. Therefore, t_{m} implies the average trap time of SMA PNPS. The parameter σ with a dimension of time measures the drop of trap probability upon deviating from the mean trap time (t_{m}). In the framework of random walk,[54] σ can be related to the number of adsorption/desorption (n) of a particle prior to being localized and the time interval between a pair of successive trials (Δt) by the relation, $\sigma = \Delta t\sqrt{n}$.

The trapping dynamics are considered to be dominated by the physicochemical properties of the lignified cell walls facing the intercell-wall spaces, which are similar at different positions along the plant stems, and hence are responsible for the similar accumulation kinetics of SMA PNPs. To be specific, lignin macromolecules bear large amount of phenyl substituents, such as hydroxyl and methoxyl groups. Therefore, the lignin polymers can interact with the aromatic and ester substituents exposed on the surface SMA PNPs via weak molecular interactions such as π-stacking and hydrogen bonding. In this relation, PNPs of different kind of polymers may exhibit different trapping dynamics, which is an issue deserving further investigation by the use of TPE-TR imaging.

The *M. exotica* plants with roots exposed to different concentration of colloidal SMA PNPs showed different rise-up time of the Eu-luminescence kinetics (Figure 9). During such lag phases, which were longer for a lower exposure concentration, the plants were active in the uptake and transport of SMA PNPs, but their accumulation in the stems were below the detection limit and hence were invisible to TPE-TR imaging. The detection limit is dependent on the size of ICCD sensing area. On the basis of the TPE-TR imaging of the diluted SMA PNP suspension (0.55 μg·mL^{-1}) in a glass capillary with a diameter comparable to the thickness of a cortex (300 μm; SI S6), the exposed area of 60 × 320 pixels for the ICCD to accommodate the image of a stem section of ~1.8 × 10 mm^2 (cf. Figure 9), and in view of the signal-to-noise ratio 0.5 for the above sensing area, we estimated a TPE-TR detection limit of ~100 particles per pixel. The is the upper limit of the TPE-TR imaging when applied to the stems because of the diffusive and scattering loss of both excitation the signal photons in the plant tissues. With the above estimated detection limit and in considering the SMA PNPs viewed by TPE-TR, we estimated that the stem section at 10−20 mm in Figure 9A accumulated ~1.8 × 10^9 particles, while the stem section at 50−60 mm in Figure 9C accumulated ~4.2 × 10^8.

The dynamics of SMA PNP uptake and translocation is case-dependent, because individual *M. exotica* plants may differ both in physical dimensions and in physiological conditions. For an instance, the characteristic uptake time t_{m} and standard deviation σ of another sample plant exposed to 55 μg·mL^{-1} were found to be ~4 h and ~1.5 h, respectively. See SI S8 for the statistics of more sample plants under different exposure concentration. It is therefore intriguing to further investigate the influence of physiological conditions of plants and physicochemical properties (polymer side substituents and particle size, and so forth) of generic PNPs on the uptake pathways and mechanisms, for which the novel TPE-TR imaging method and analytical protocol established in the present work can be powerful means.

■ ASSOCIATED CONTENT

Ⓢ Supporting Information

The Supporting Information is available free of charge on the ACS Publications website at DOI: 10.1021/acs.est.8b05689.

> Chemical structures, additional autofluorescence imaging data, characterization of TPE-TR imaging depth, methods for morphological analysis and luminescence intensity plot, TPE-TR imaging of colloidal SMA PNPs in capillary, and an additional case study of TPE-TR imaging (PDF)
>
> Video of the detailed spatiotemporal evolution (AVI)

■ AUTHOR INFORMATION

Corresponding Authors

*Tel: +86-10-62516604; e-mail: lmfu@ruc.edu.cn (L.-M.F.).
*Tel: +86-10-62516604; e-mail: jpzhang@ruc.edu.cn (J.-P.Z.).

ORCID

Jian-Ping Zhang: 0000-0002-9216-2386

Notes

The authors declare no competing financial interest.

■ ACKNOWLEDGMENTS

This work was supported by National Natural Science Foundation of China (NSFC, Grant Nos. 21673288 and 21227803) and National Key R&D Program of China (Grant No. 2018YFA0208701).

■ REFERENCES

(1) Colvin, V. L. The potential environmental impact of engineered nanomaterials. *Nat. Biotechnol.* **2003**, *21* (10), 1166−1170.

(2) Benson, W. H.; Gallagher, K.; McClintock, J. T. US Environmental protection agency's activities to prepare for regulatory and risk assessment applications of genomics information. *Environ. Mol. Mutagen.* **2007**, *48* (5), 359−362.

(3) Nel, A.; Xia, T.; Madler, L.; Li, N. Toxic potential of materials at the nanolevel. *Science* **2006**, *311* (5761), 622−627.

(4) von der Kammer, F.; Ferguson, P. L.; Holden, P. A.; Masion, A.; Rogers, K. R.; Klaine, S. J.; Koelmans, A. A.; Horne, N.; Unrine, J. M. Analysis of engineered nanomaterials in complex matrices (environment and biota): General considerations and conceptual case studies. *Environ. Toxicol. Chem.* **2012**, *31* (1), 32−49.

(5) Gottschalk, F.; Nowack, B. The release of engineered nanomaterials to the environment. *J. Environ. Monit.* **2011**, *13* (5), 1145−1155.

(6) Dunford, R.; Salinaro, A.; Cai, L. Z.; Serpone, N.; Horikoshi, S.; Hidaka, H.; Knowland, J. Chemical oxidation and DNA damage catalysed by inorganic sunscreen ingredients. *FEBS Lett.* **1997**, *418* (1−2), 87−90.

(7) Cui, D. X.; Tian, F. R.; Ozkan, C. S.; Wang, M.; Gao, H. J. Effect of single wall carbon nanotubes on human HEK293 cells. *Toxicol. Lett.* **2005**, *155* (1), 73−85.

(8) Braydich-Stolle, L.; Hussain, S.; Schlager, J. J.; Hofmann, M. C. In vitro cytotoxicity of nanoparticles in mammalian germline stem cells. *Toxicol. Sci.* **2005**, *88* (2), 412−419.

(9) Michalet, X.; Pinaud, F. F.; Bentolila, L. A.; Tsay, J. M.; Doose, S.; Li, J. J.; Sundaresan, G.; Wu, A. M.; Gambhir, S. S.; Weiss, S. Quantum dots for live cells, in vivo imaging, and diagnostics. *Science* **2005**, *307* (5709), 538−544.

(10) Navarro, E.; Piccapietra, F.; Wagner, B.; Marconi, F.; Kaegi, R.; Odzak, N.; Sigg, L.; Behra, R. Toxicity of silver nanoparticles to *Chlamydomonas reinhardtii. Environ. Sci. Technol.* **2008**, *42* (23), 8959−8964.

(11) Hatami, M.; Kariman, K.; Ghorbanpour, M. Engineered nanomaterial-mediated changes in the metabolism of terrestrial plants. *Sci. Total Environ.* **2016**, *571*, 275−291.

(12) Andrady, A. L. Microplastics in the marine environment. *Mar. Pollut. Bull.* **2011**, *62* (8), 1596−1605.

(13) Rochman, C. M.; Browne, M. A.; Halpern, B. S.; Hentschel, B. T.; Hoh, E.; Karapanagioti, H. K.; Rios-Mendoza, L. M.; Takada, H.; Teh, S.; Thompson, R. C. Classify plastic waste as hazardous. *Nature* **2013**, *494* (7436), 169−171.

(14) Cole, M.; Lindeque, P. K.; Fileman, E.; Clark, J.; Lewis, C.; Halsband, C.; Galloway, T. S. Microplastics alter the properties and sinking rates of zooplankton faecal pellets. *Environ. Sci. Technol.* **2016**, *50* (6), 3239−3246.

(15) Browne, M. A.; Dissanayake, A.; Galloway, T. S.; Lowe, D. M.; Thompson, R. C. Ingested microscopic plastic translocates to the circulatory system of the mussel, *Mytilus edulis* (L.). *Environ. Sci. Technol.* **2008**, *42* (13), 5026−5031.

(16) Gigault, J.; ter Halle, A.; Baudrimont, M.; Pascal, P.-Y.; Gauffre, F.; Phi, T.-H.; El Hadri, H.; Grassl, B.; Reynaud, S. Current opinion: What is a nanoplastic? *Environ. Pollut.* **2018**, *235*, 1030−1034.

(17) Hernandez, L. M.; Yousefi, N.; Tufenkji, N. Are there nanoplastics in your personal care products? *Environ. Sci. Technol. Lett.* **2017**, *4* (7), 280−285.

(18) Alimi, O. S.; Budarz, J. F.; Hernandez, L. M.; Tufenkji, N. Microplastics and nanoplastics in aquatic environments: aggregation, deposition, and enhanced contaminant transport. *Environ. Sci. Technol.* **2018**, *52* (4), 1704−1724.

(19) Chen, C. S.; Le, C.; Chiu, M. H.; Chin, W. C. The impact of nanoplastics on marine dissolved organic matter assembly. *Sci. Total Environ.* **2018**, *634*, 316−320.

(20) Gigault, J.; Pedrono, B.; Maxit, B.; Ter Halle, A. Marine plastic litter: the unanalyzed nano-fraction. *Environ. Sci.: Nano* **2016**, 3 (2), 346−350.

(21) Mattsson, K.; Ekvall, M. T.; Hansson, L. A.; Linse, S.; Malmendal, A.; Cedervall, T. Altered behavior, physiology, and metabolism in fish exposed to polystyrene nanoparticles. *Environ. Sci. Technol.* **2015**, *49* (1), 553−561.

(22) Oriekhova, O.; Stoll, S. Heteroaggregation of nanoplastic particles in the presence of inorganic colloids and natural organic matter. *Environ. Sci.: Nano* **2018**, *5* (3), 792−799.

(23) Li, K.; Ding, D.; Huo, D.; Pu, K. Y.; Thao, N. N. P.; Hu, Y.; Li, Z.; Liu, B. Conjugated polymer based nanoparticles as dual-modal probes for targeted in vivo fluorescence and magnetic resonance imaging. *Adv. Funct. Mater.* **2012**, *22* (15), 3107−3115.

(24) Graf, N.; Bielenberg, D. R.; Kolishetti, N.; Muus, C.; Banyard, J.; Farokhzad, O. C.; Lippard, S. J. $\alpha_V\beta_3$ integrin-targeted PLGA-PEG nanoparticles for enhanced anti-tumor efficacy of a Pt(IV) Prodrug. *ACS Nano* **2012**, *6* (5), 4530−4539.

(25) Oberdorster, G.; Oberdorster, E.; Oberdorster, J. Nanotoxicology: An emerging discipline evolving from studies of ultrafine particles. *Environ. Health Perspect.* **2005**, *113* (7), 823−839.

(26) Velzeboer, I.; Kwadijk, C. J. A. F.; Koelmans, A. A. Strong sorption of PCBs to nanoplastics, microplastics, carbon nanotubes, and fullerenes. *Environ. Sci. Technol.* **2014**, *48* (9), 4869−4876.

(27) Bouwmeester, H.; Hollman, P. C. H.; Peters, R. J. B. Potential health impact of environmentally released micro- and nanoplastics in the human food production chain: experiences from nanotoxicology. *Environ. Sci. Technol.* **2015**, *49* (15), 8932−8947.

(28) Hoet, P. H. M.; Nemmar, A.; Nemery, B. Health impact of nanomaterials? *Nat. Biotechnol.* **2004**, *22* (1), 19−19.

(29) Chung, H.; Kim, M. J.; Ko, K.; Kim, J. H.; Kwon, H.; Hong, I.; Park, N.; Lee, S. W.; Kim, W. Effects of graphene oxides on soil enzyme activity and microbial biomass. *Sci. Total Environ.* **2015**, *514*, 307−313.

(30) Cozar, A.; Echevarria, F.; Gonzalez-Gordillo, J. I.; Irigoien, X.; Ubeda, B.; Hernandez-Leon, S.; Palma, A. T.; Navarro, S.; Garcia-de-Lomas, J.; Ruiz, A.; Fernandez-de-Puelles, M. L.; Duarte, C. M. Plastic debris in the open ocean. *Proc. Natl. Acad. Sci. U. S. A.* **2014**, *111* (28), 10239−10244.

(31) Lopez-Luna, J.; Silva-Silva, M. J.; Martinez-Vargas, S.; Mijangos-Ricardez, O. F.; Gonzalez-Chavez, M. C.; Solis-Dominguez, F. A.; Cuevas-Diaz, M. C. Magnetite nanoparticle (NP) uptake by wheat plants and its effect on cadmium and chromium toxicological behavior. *Sci. Total Environ.* **2016**, *565*, 941−950.

(32) Raliya, R.; Nair, R.; Chavalmane, S.; Wang, W. N.; Biswas, P. Mechanistic evaluation of translocation and physiological impact of titanium dioxide and zinc oxide nanoparticles on the tomato (*Solanum lycopersicum* L.) plant. *Metallomics* **2015**, 7 (12), 1584−1594.

(33) Koo, Y.; Wang, J.; Zhang, Q.; Zhu, H.; Chehab, E. W.; Colvin, V. L.; Alvarez, P. J. J.; Braam, J. Fluorescence reports intact quantum dot uptake into roots and trans location to leaves of *Arabidopsis thaliana* and subsequent ingestion by insect herbivores. *Environ. Sci. Technol.* **2015**, *49* (1), 626−632.

(34) Peng, J.; Sun, Y.; Liu, Q.; Yang, Y.; Zhou, J.; Feng, W.; Zhang, X.; Li, F. Upconversion nanoparticles dramatically promote plant growth without toxicity. *Nano Res.* **2012**, *5* (11), 770−782.

(35) Wang, H.; Kou, X.; Pei, Z.; Xiao, J. Q.; Shan, X.; Xing, B. Physiological effects of magnetite (Fe3O4) nanoparticles on perennial ryegrass (Lolium perenne L.) and pumpkin (Cucurbita mixta) plants. *Nanotoxicology* **2011**, *5* (1), 30−42.

(36) Hernandez-Viezcas, J. A.; Castillo-Michel, H.; Andrews, J. C.; Cotte, M.; Rico, C.; Peralta-Videa, J. R.; Ge, Y.; Priester, J. H.; Holden, P. A.; Gardea-Torresdey, J. L. In situ synchrotron x-ray fluorescence mapping and speciation of ceo2 and zno nanoparticles in soil cultivated soybean (glycine max). *ACS Nano* **2013**, 7 (2), 1415−1423.

(37) Zhu, H.; Han, J.; Xiao, J. Q.; Jin, Y. Uptake, translocation, and accumulation of manufactured iron oxide nanoparticles by pumpkin plants. *J. Environ. Monit.* **2008**, *10* (6), 713−717.

(38) Lin, S.; Reppert, J.; Hu, Q.; Hudson, J. S.; Reid, M. L.; Ratnikova, T. A.; Rao, A. M.; Luo, H.; Ke, P. C. Uptake, translocation, and transmission of carbon nanomaterials in rice plants. *Small* **2009**, *5* (10), 1128−1132.

(39) Chen, R.; Ratnikova, T. A.; Stone, M. B.; Lin, S.; Lard, M.; Huang, G.; Hudson, J. S.; Ke, P. C. Differential uptake of carbon nanoparticles by plant and mammalian cells. *Small* **2010**, *6* (5), 612−617.

(40) Chen, Z.; Wu, X.; Hu, S.; Hu, P.; Yan, H.; Tang, Z.; Liu, Y. Multicolor upconversion $NaLuF_4$ fluorescent nanoprobe for plant cell imaging and detection of sodium fluorescein. *J. Mater. Chem. C* **2015**, 3 (1), 153−161.

(41) Jiang, X.; Tian, L.; Ma, Y.; Ji, R. Quantifying the bioaccumulation of nanoplastics and pahs in the clamworm Perinereis aibuhitensis. *Sci. Total Environ.* **2019**, *655*, 591−597.

(42) Cole, M.; Lindeque, P.; Fileman, E.; Halsband, C.; Goodhead, R.; Moger, J.; Galloway, T. S. Microplastic ingestion by zooplankton. *Environ. Sci. Technol.* **2013**, *47* (12), 6646−6655.

(43) Lee, W. S.; Cho, H.-J.; Kim, E.; Huh, Y. H.; Kim, H.-J.; Kim, B.; Kang, T.; Lee, J.-S.; Jeong, J. Bioaccumulation of polystyrene nanoplastics and their effect on the toxicity of Au ions in zebrafish embryos. *Nanoscale* **2019**; DOI: 10.1039/C8NR09321K.

(44) Al-Sid-Cheikh, M.; Rowland, S. J.; Stevenson, K.; Rouleau, C.; Henry, T. B.; Thompson, R. C. Uptake, Whole-body distribution, and depuration of nanoplastics by the scallop pecten maximus at environmentally realistic concentrations. *Environ. Sci. Technol.* **2018**, *52* (24), 14480−14486.

(45) Zhang, C. J.; Wang, C. X.; Gao, Z. Y.; Ke, C.; Fu, L. M.; Zhang, Z.; Wang, Y.; Zhang, J.-P. Wide field of view, real time bioimaging apparatus for noninvasive analysis of nanocarrier pharmacokinetics in living model animals. *Rev. Sci. Instrum.* **2018**, *89*, (8); 085105.

(46) Bonilla-Bird, N. J.; Paez, A.; Reyes, A.; Hernandez-Viezcas, J. A.; Li, C.; Peralta-Videa, J. R.; Gardea-Torresdey, J. L. Two-photon microscopy and spectroscopy studies to determine the mechanism of copper oxide nanoparticle uptake by sweetpotato roots during postharvest treatment. *Environ. Sci. Technol.* **2018**, *52* (17), 9954−9963.

(47) Yang, W.; Fu, L. M.; Wen, X.; Liu, Y.; Tian, Y.; Liu, Y. C.; Han, R. C.; Gao, Z. Y.; Wang, T. E.; Sha, Y. L.; Jiang, Y. Q.; Wang, Y.; Zhang, J.-P. Nanoprobes for two-photon excitation time-resolved imaging of living animals: In situ analysis of tumor-targeting dynamics of nanocarriers. *Biomaterials* **2016**, *100*, 152−161.

(48) He, S. D.; Yang, X.-T.; Yan, C. C.; Jiang, Z.; Yu, S. H.; Zhou, Y. Y.; Jia, L. Promising compounds from murraya exotica for cancer metastasis chemoprevention. *Integr. Cancer Ther.* **2017**, *16* (4), 556−562.

(49) Huang, R. L.; Li, Z. H.; Wang, S. Y.; Fu, J. T.; Cheng, D. M.; Zhang, Z. X. Insecticidal effect of volatile compounds from plant materials of *Murraya exotica* against red imported fire ant workers. *Sociobiology* **2016**, *63* (2), 783−791.

(50) Xue, F.; Ma, Y.; Fu, L.; Hao, R.; Shao, G.; Tang, M.; Zhang, J.; Wang, Y. A europium complex with enhanced long-wavelength sensitized luminescent properties. *Phys. Chem. Chem. Phys.* **2010**, *12* (13), 3195−3202.

(51) Barros, J.; Serk, H.; Granlund, I.; Pesquet, E. The cell biology of lignification in higher plants. *Ann. Bot.* **2015**, *115* (7), 1053−1074.

(52) Gibson, L. J. The hierarchical structure and mechanics of plant materials. *J. R. Soc., Interface* **2012**, *9* (76), 2749−2766.

(53) Burgess, S. S. O.; Adams, M. A.; Turner, N. C.; Beverly, C. R.; Ong, C. K.; Khan, A. A. H.; Bleby, T. M. An improved heat pulse method to measure low and reverse rates of sap flow in woody plants. *Tree Physiol.* **2001**, *21* (9), 589−598.

(54) Giddings, J. C. The random downstream migration of molecules in chromatography. *J. Chem. Educ.* **1958**, *35* (12), 588−591.